RSC Advances

PAPER

View Article Online
View Journal | View Issue

Cite this: *RSC Adv.*, 2017, **7**, 45177

A flower-like NiO–SnO_2 nanocomposite and its non-enzymatic catalysis of glucose

Yan Zhou,[a] Xiao Ni,[a] Zhen Ren,[a] Jiayi Ma,[a] Jinzhong Xu[b] and Xiaojun Chen *[a]

A flower-like NiO–SnO_2 nanocomposite (NSNF) with electrochemical activity was synthesized by a solvothermal method. The morphology and composition of the NSNF have been characterized by transmission electron microscopy (TEM), scanning electron microscopy (SEM) and X-ray diffraction (XRD). The synthesized NSNF was immobilized onto the surface of an indium tin oxide (ITO) electrode and exhibited highly non-enzymatic catalysis towards the oxidation of glucose. The effect of NaOH concentration on the oxidation performance of glucose was investigated. Under the optimum conditions, the catalytic current showed a linear relationship with the increase of glucose concentration in the range of 0.01–26 mM, with a detection limit of 1 μM. The excellent sensing performance can be attributed to the unique porous architecture of NSNF, which enhanced the electron transfer during the electrochemical sensing of glucose. The glucose sensor also had a high selectivity for glucose detection, which could effectively resist the interference from ascorbic acid (AA), uric acid (UA), citric acid (CA), hydrogen peroxide (H_2O_2) and even other carbohydrates, such as fructose, sucrose and maltose. Finally, the glucose sensor was also used for glucose detection in real human serum samples and the results were satisfactory.

Received 10th July 2017
Accepted 13th September 2017

DOI: 10.1039/c7ra07582k

rsc.li/rsc-advances

1. Introduction

Glucose is an important compound in human life processes and the analysis and testing of glucose are of great importance in a variety of fields, including biotechnology, clinical diagnosis and food industry, *etc.*[1,2] Although various potential approaches such as acoustic, fluorescence, optical, electronic and transdermal technologies have been explored for glucose detection, electrochemical glucose biosensors have attracted much attention due to their high sensitivity, low detection limit and low cost.[3–6] Generally, electrochemical sensors for glucose determination are classified into enzymatic and non-enzymatic types. Conventional electrochemical glucose sensors are normally fabricated based on the use of glucose oxidase (GOD), which has showed high selectivity and sensitivity for glucose.[7–9] However, enzymatic biosensors often exhibit instability and unsatisfactory reproducibility due to the influence from the surrounding conditions such as temperature and pH.[10,11] Therefore, non-enzymatic glucose sensors are highly desirable based on the direct oxidation of glucose on the electrode surface without using the fragile enzymes.

During the past few years, nanomaterials have been widely used in the fabrication of electrochemical sensors due to their good conductivity and catalytic activity. Meanwhile, noble metal materials like Au[12] and Pt[13,14] have been explored as the electrode modifications towards the oxidation of glucose. However, these novel metals are so expensive that various metal oxides such as WO_3, Co_3O_4 and NiO are emerged as the economical substitutes.[15,16] Among all, NiO is highly suitable for the fabrication of non-enzymatic glucose sensors, owing to the excellent catalytic activity, low toxicity and abundant sources.[17,18] Razium Ali Soomro *et al.* prepared an enzyme-free glucose sensor using novel hedgehog-like NiO nanostructures.[19] R. Prasad *et al.* also applied nickel-oxide multiwall carbon-nanotube/reduced graphene oxide a ternary composite for enzymefree glucose sensing.[20]

In addition, porous nanomaterials are promising candidates for electrode modifications, since they can provide a large active surface for mass transport and electron transfer.[21] Lu *et al.* prepared a nanoporous Ag catalyst by a dealloying process;[22] another nanostructured porous Ag electrode was also reported by Wang *et al.*, which had been applied in the electrochemical reduction of CO_2.[23] Herein, we demonstrate a novel electrochemical non-enzymatic glucose sensor based on porous NiO–SnO_2 nanocomposite.

In this work, a flower-like NiO–SnO_2 nanostructure (NSNF) was synthesized using a template-free hydrothermal method, and followed by a calcination process.[24] In order to study the non-enzymatic electrocatalysis of NSNF towards glucose, the sensor performances including the sensitivity, selectivity, stability, linear response range and limit of detection (LOD) were systematically investigated. This newly built glucose sensor has also been used for the determination of glucose in human serum samples.

[a]*College of Chemistry and Molecular Engineering, Nanjing Tech University, Nanjing, 211800, PR China. E-mail: chenxj@njtech.edu.cn*
[b]*Jiangsu Sinography Testing Co. Ltd., Nanjing, 210032, PR China*

2. Experimental

2.1 Chemicals

Nickel chloride hexahydrate ($NiCl_2 \cdot 6H_2O$), tin(II) chloride dihydrate ($SnCl_2 \cdot 2H_2O$), thiourea (NH_2CSNH_2, TU), ethylene glycol, ethanol, sodium hydroxide (NaOH), uric acid (UA), ascorbic acid (AA), hydrogen peroxide (H_2O_2) and citric acid (CA), the human serum samples were provided by Jiangsu Center for Clinical Laboratory (JSCCL). Perfluorosulfonic acid (Nafion, 5 wt%) was purchased from DuPont, and diluted to 0.5 wt% for use. The experimental water was double distilled water. All reagents were of analytical grade and used as received without further purification.

2.2 Apparatus

The morphology of NSNF was observed by transmission electron microscopy (TEM, JEOL JEM-200CX), scanning electron microscopy (FESEM, Hitachi S4800) and a powder X-ray diffraction (XRD, Rigaku Smartlab). Cyclic voltammograms (CVs) were performed with a CHI 660D analyzer (Shanghai Chenhua Instrument Co., China). All experiments were conducted using a three-electrode electrochemical system with a modified ITO working electrode (Φ = 3 mm), a saturated calomel reference electrode (SCE) and a platinum slice counter electrode.

The working electrode was prepared by dropping 10 μL of 1 mg mL^{-1} NSNF dispersion in 0.5 wt% of Nafion onto a precleaned ITO electrode and then let it dried in air at room temperature. The detection of glucose was carried out in 0.1 M of NaOH, and the current response of the sensor was the subtraction of total current and the background ($\Delta i = i_p - i_0$).

2.3 Synthesis of NSNF

In a typical synthesis process,[24] 0.1128 g of $SnCl_2 \cdot 2H_2O$ and 0.1782 g of $NiCl_2 \cdot 6H_2O$ were added into 45 mL of ethylene glycol to form a homogeneous solution. Subsequently, 0.22 g of thiourea was added with vigorous stirring at 30 °C for 10 min, resulting in a green precipitate. The mixture was then sealed in a Teflon lined stainless-steel autoclave and maintained at 245 °C for 24 h. After cooling naturally to room temperature, the solution emitted pungent odor and the resulting black product was collected by centrifugation and washed for 6 times with distilled water and absolute ethanol. The as-prepared flower-like nickel tin sulfur structures were annealed at 650 °C for 2 h in air to remove part of sulfur and oxidize Ni and Sn to NiO and SnO_2, and the light green colored product was designated as NSNF. NiO or SnO_2 was also prepared as comparison using the same procedure, with single $NiCl_2 \cdot 6H_2O$ or $SnCl_2 \cdot 2H_2O$ as the precursor.

3. Results and discussion

3.1 Structure and morphology

The SEM image of NSNF was shown in Fig. 1A, which was a flower-like structure with the average size of 2.2 μm. Observed from the many small particles and slices scattering around, it was supposed that NSNF structure was actually formed by assembling many small particles. EDS analysis (Fig. 1B) showed that the elemental molar ratio of Ni, Sn and O in NSNF was 19.52 : 11.42 : 59.82. This suggested that most of the Ni and Sn were oxidized in the annealing process, and most of the sulfur atoms had been removed. Furthermore, during the calcination process, NiO and SnO_2 crystals would nucleate, grow and aggregate to form NSNF under a moderate calcination temperature (in this case, 650 °C) without further chemical leaching or gas reduction. In addition, these structures were sufficiently stable that they could not be broken into discrete nanosheets, even after ultrasonication for a long time. Fig. 1C was the TEM image of NSNF, and it could be seen that NSNF had many pores, which greatly increased the specific surface area. The crystal phases of SnO_2 (curve a), NiO (curve c) and NSNF (curve b) were characterized by XRD, and the data was shown in Fig. 1D. In curve a, tetragonal phase SnO_2 (JCPDS card no. 77-0451) showed diffraction peaks at 2θ = 24.8, 31.4 and 52.0°, relating to the 110, 101 and 211 planes.[24] In curve c, 200, 111, and 220 planes of cubic phase NiO (JCPDS card no. 75-0197) appeared at 2θ = 37.2, 42.3 and 66.6°.[25] With regard to the curve b, in the NSNF, there existed simultaneously the 110, 101 and 211 crystal planes from tetragonal SnO_2, and the 200, 111 and 220 crystal planes from cubic NiO. In terms of the diffraction peak intensity, the NSNF crystal structure was mainly attributed to SnO_2. Thus, we calculated the average grain size of NSNF with 101 plane by Scherer formula:[24] $D = 0.9\ \lambda/\beta \cos\theta$, where λ is the wavelength of the X-ray beam, β is the full width at half maximum (FWHM) and θ is the diffraction angle. The mean crystallite size of the as-prepared NSNF was calculated to be 0.42 nm. Therefore, the SEM result was further confirmed that the NSNF porous material was essentially formed by numerous small particles.

3.2 Growth mechanisms of NSNF

Formation mechanism of nanoflower structure is complicated and greatly depends on various parameters such as time, temperature, hydrophobic or hydrophilic interactions, hydrogen bonding, electrostatic and van der Walls forces, crystal-face attraction, dipolar fields, and Ostwald ripening, *etc.*[26]

In order to understand the growth mechanism of NSNF, the solvothermal reactions with different time were investigated, such as 12, 24, 28 and 32 h, respectively. The corresponding SEM images of nickel tin sulfur precursors were shown in Fig. 2. When the reaction time was 12 h, the prototype of NSNF was already formed with the diameter of about 1 μm (Fig. 2A). The number of petals was relative small compared with the final product of NSNF. The SEM image of the product with the reaction time of 24 h was shown in Fig. 2B. The flower-like structure was full-developed with more pores and the size was increased to about 2.2 μm. In addition, we also found that the petals were much smoother than those shown in Fig. 1A, indicating the calcination process enhanced the porosity along with the release of SO_2. EDS analysis also conducted, and the elemental molar ratio of Ni, Sn, S and O was 12.44 : 10.57 : 29.62 : 47.34, suggesting that the possible coexistence of NiS, SnS, SnS_2, NiO and SnO_2 in the system. The

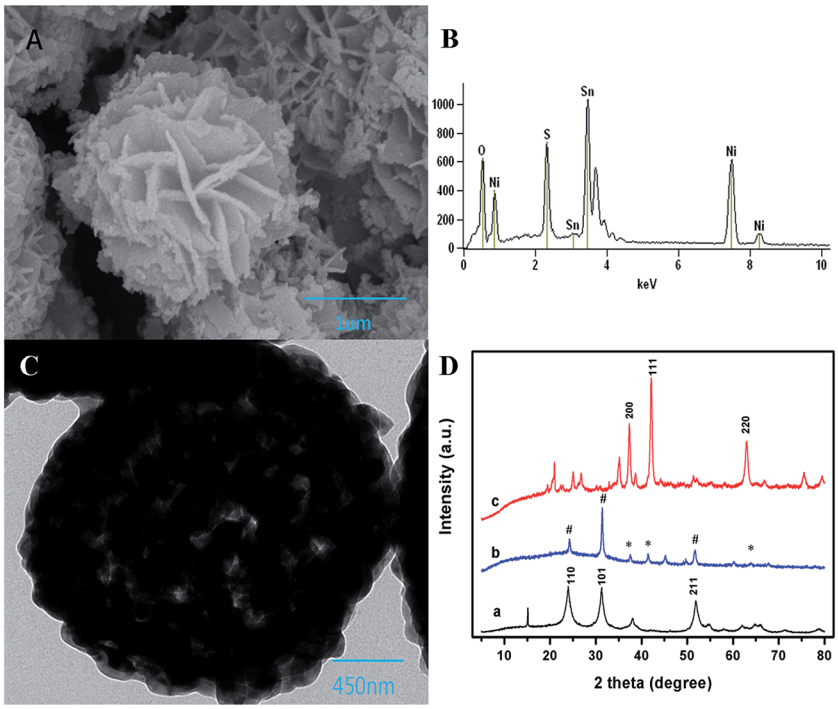

Fig. 1 (A) SEM, (B) EDS, and (C) TEM characterization of NSNF; (D) XRD curves of (a) NiO, (b) NSNF and (c) SnO_2. In the curve b, the NiO and SnO_2 peaks are marked with asterisks and pound signs, respectively.

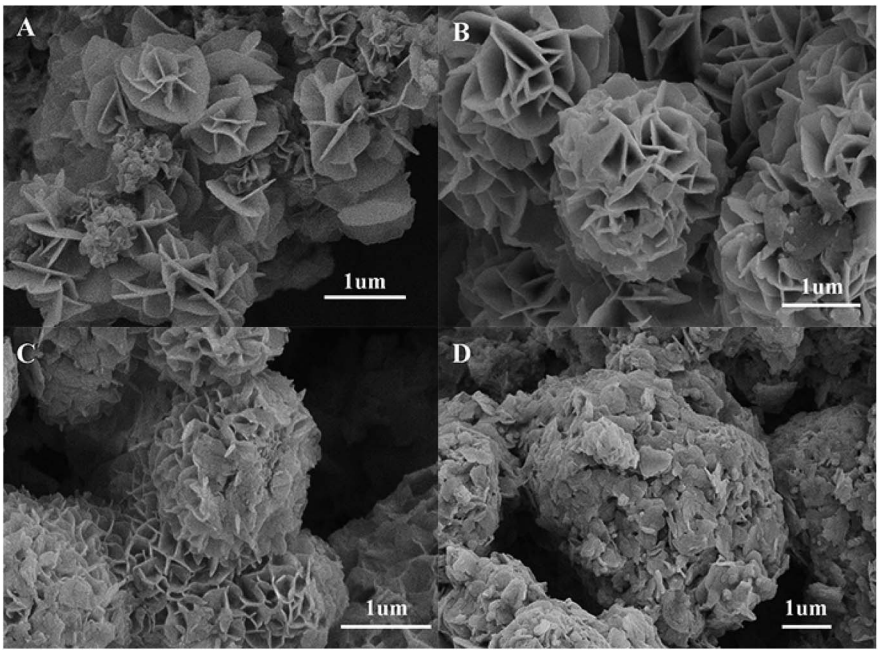

Fig. 2 SEM images of nickel tin sulfur precursors of different solvothermal reaction time: (A) 12 h, (B) 24 h, (C) 28 h and (D) 32 h, respectively.

sulphur content is much higher in nickel tin sulfur precursor than that in NSNF. When the reaction time was extended to 28 h (Fig. 2C) and even 32 h (Fig. 2D), it could be found that the pores were blocked by the flaky particles and the former monodispersed nano flowers were fused gradually, which might be due to the Ostwald ripening. As shown in Fig. 2D, the porous flower-like structure almost disappeared, and the particle size was larger than 5 μm. Thus, the optimal solvothermal reaction time was chosen as 24 h in this work.

We also supposed the growth mechanism of NSNF as follows: raw materials firstly developed into flaky particles, which could assemble themselves into a flower-like porous structure

afterwards during the following several hours.[27] During this process, TU played an important role in the nucleation: (1) TU is used as sulfur source, which was thermally decomposed to produce H_2S, and then H_2S reacted with Ni^{2+} and Sn^{2+} to produce NiS and SnS; (2) TU is used as a complexing agent to produce $Sn(TU)_x^{2+}$ and $Ni(TU)_x^{2+}$, which slowed down the nucleation and growth rate of NiS and SnS, making the particle size smaller and facilitating the formation of flower-like morphology. Additionally, the solvent ethylene glycol decomposed at high temperature and released oxygen, increasing the porosity of the materials and oxidizing SnS to SnS_2 or SnO_2 partially. Thus, the relative equations during the formation process of the nickel–tin–sulfur precursor were summarized as follows:

$$TU + 2H_2O = CO_2 + 2NH_3 + H_2S$$

$$Sn^{2+} + S^{2-} = SnS$$

$$Ni^{2+} + S^{2-} = NiS$$

$$Sn^{2+} + xTU \rightarrow Sn(TU)_x^{2+}$$

$$Ni^{2+} + xTU \rightarrow Ni(TU)_x^{2+}$$

$$Sn(TU)_x^{2+} + S^{2-} \rightarrow SnS + xTU$$

$$Ni(TU)_x^{2+} + S^{2-} \rightarrow NiS + xTU$$

$$2OHCH_2CH_2OH \rightarrow 2CH_2{=}CH_2 + 2H_2O + O_2$$

$$SnS + O_2 \rightarrow SnS_2 + SO_2$$

$$SnS + 2O_2 \rightarrow SnO_2 + SO_2$$

The formation process of the nickel tin sulfur precursor was also illustrated in Scheme 1. After the as-prepared flower-like nickel tin sulfur precursor was calcinated at 650 °C for 2 h, most sulfur was removed, and NiS and SnS were turned into NiO and SnO_2, respectively:

$$SnS + 2O_2 \rightarrow SnO_2 + SO_2$$

$$2NiS + 3O_2 \rightarrow 2NiO + 2SO_2$$

3.3 Electrocatalytic oxidation of glucose at the different modified electrodes

The electrocatalytic activities of the constructed NiO, SnO_2 and NSNF modified electrodes were all characterized. As shown in Fig. 3A, the CVs of NiO/ITO under successive addition of the glucose solution from 0–2.0 mM were recorded. In curve a, there was a pair of redox peaks with the anodic and cathodic peak potentials of 0.520 and 0.425 V, respectively in the absence of glucose, corresponding to the transform of Ni(II)/Ni(III).[28] With the increase of glucose concentration (curve b to g), the oxidation peak current gradually increased and the peak potential positively shifted, indicating that NiO had a significant catalytic effect on glucose. Fig. 3B showed the CVs of SnO_2/ITO in the absence (curve a) and presence of different concentrations of glucose solution (curve b to g) under the same conditions. However, no obvious redox peaks were seen in curve a and nearly tiny increase in the peak currents from curve b to g, illustrating that SnO_2 could hardly catalyze the oxidation of glucose.

Fig. 3C represented the CVs of NiO/ITO (curve a and a′), SnO_2/ITO (curve b and b′) and NSNF/ITO (curve c and c′) in the absence and presence of 1.0 mM glucose in 0.1 M NaOH solution. We found that compared with NiO and NSNF, the catalytic effect of SnO_2 on glucose was almost negligible. The catalytic current (Δi) obtained on NSNF was nearly 3 times larger than that on NiO, and the oxidation peak potential was also negatively shifted by 0.03 V, indicating NSNF could enhance the electrocatalytic oxidation of glucose. This might be owing to two reasons: (1) the porous structure of NSNF could greatly accelerate the electron transfer and mass transfer inside the composite; (2) SnO_2-based skeleton structure promoted the dispersity of NiO nanoparticles, which could enhance the catalytic activity of NiO towards glucose.

3.4 Effect of NaOH concentration

An alkaline medium is often required for enhancing the electrocatalytic activity of transition metals for oxidation of carbohydrate compound.[29] The oxidation of glucose to glucolactone on the electrode surface was electro-catalyzed by the Ni(II)/Ni(III) redox couple, which can be illustrated as the following electrochemical reaction:[28]

$$Ni(II) + OH^- \rightarrow Ni(III) + e^-$$

$$Ni(III) + \text{glucose} \rightarrow Ni(II) + \text{glucolactone}$$

In this electrochemical catalytic reaction, Ni(II) was firstly oxidized to Ni(III) with the involvement of OH^-, and then Ni(III) oxidized the glucose to glucolactone with the reduction of Ni(III) to Ni(II) simultaneously.

In the presence of glucose, the oxidation current of Ni(II) was increased. In order to screen for the optimal concentration of

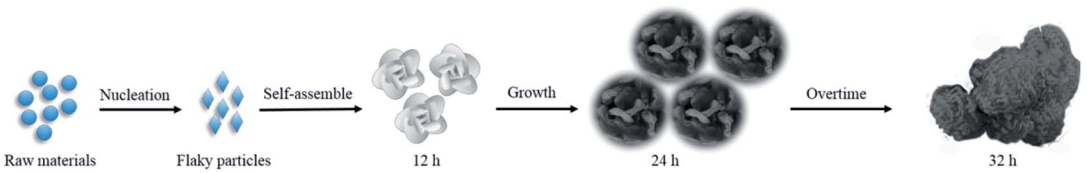

Scheme 1 The illustration of the growth process of nickel tin sulfur precursor.

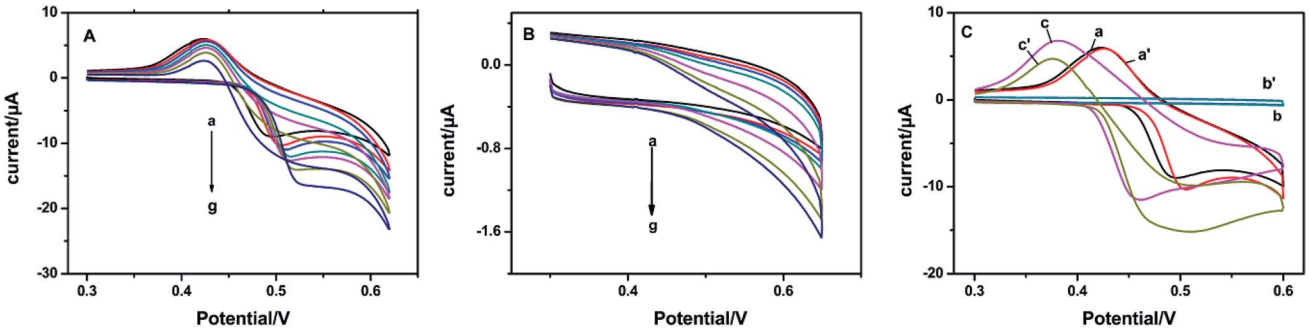

Fig. 3 CVs of (A) NiO/ITO and (B) SnO_2/ITO in 0.1 M NaOH solution with (from a to g) 0, 0.1, 0.2, 0.4, 0.6, 1.0, 1.5, and 2.0 mM glucose at a scan rate of 100 mV s^{-1}. (C) CVs of NiO/ITO (curves of a and a′), SnO_2/ITO (curves of b and b′), and NSNF/ITO (c and c′) in 0.1 M NaOH without and with 1.0 mM glucose at a scan rate of 50 mV s^{-1}.

NaOH for the glucose detection, the catalytic performance of NSNF/ITO was investigated in different NaOH concentrations ranging from 0.05 to 0.4 M, under the successive addition of the glucose solution from 0.2 to 15.0 mM. The results were shown in Fig. 4. It could be seen that in all concentrations of NaOH solution, the Δi value increased with the increase of glucose concentration, and the sensitivity in 0.1 M NaOH was the highest. The more concentrated NaOH brought down the sensitivity, due to the redundant OH^- might block the electro-adsorption of glucose.[30] Thus, 0.1 M of NaOH solution was considered as the optimal supporting electrolyte.

3.5 Amperometric analysis

The effective surface area (ESA) of working electrodes plays an important role in the development of chemical sensors because it directly influences their sensitivity. The ESA can be estimated in several ways.[31,32] Herein, CVs of NSNF/ITO and Nf modified ITO (blank ITO) were recorded in 5 mM $K_3Fe(CN)_6$ solution containing 0.1 M KCl, respectively. As shown in Fig. 5A, the i_p values of NSNF/ITO and Nf modified ITO (blank ITO) both increased linearly with the square root of the scan rates ($v^{1/2}$). This suggests that the reactions occurring on the electrode are nearly reversible and implies that the mass transfer phenomenon in the double layer region of the electrodes is mainly controlled by diffusion.[33] Thus, the ESA of working electrode can be determined using Randles–Sevcik equation:

$$i_p = 2.69 \times 10^5 n^{3/2} A D^{1/2} v^{1/2} C$$

where n is the number of electron involving in the redox process, D is the diffusion coefficient of $Fe(CN)_6^{3-}$ (1×10^{-5} cm^2 s^{-1}), C is the concentration of the probe molecule in the solution (mol cm^{-3}), v is the scan rate (V s^{-1}) and i_p is the peak current of the redox couple (A). The ratio of i_p to $v^{1/2}$ corresponds to the Randles' slope. The ESA of NSNF/ITO and blank ITO were calculated as 0.0705 and 8.06×10^{-3} cm^2, respectively, showing the modification of NSNF could enhance the ESA by about 8.75 times.

We also investigated the effect of scan rate on the catalytic performance of NSNF/ITO. Fig. 5B shows the CVs of NSNF/ITO recorded at different scan rates from 30 to 100 mV s^{-1} in 0.1 M NaOH solution containing 1.0 mM of glucose. A pair of peaks with the anodic and cathodic peak potentials of 0.500 and 0.375 V, respectively at the scan rate of 50 mV s^{-1}. Both the anodic and cathodic i_p grew linearly with the $v^{1/2}$, indicating a surface-controlled electrochemical process, as shown in the inset.

Fig. 5C showed the CV curves recorded of the as-prepared sensor on successive addition of glucose. As the glucose was added into the 0.1 M NaOH solution, the sensor responded rapidly to the substrates. The oxidation peak current of NSNF increased as the concentration of glucose increased from 0.01 to 26 mM; and accordingly, the reduction peak current continuously decreased. Fig. 5D gave the corresponding equation Δi (μA) $= -0.0243 - 0.9945 C_{glucose}$ (mM) ($R = 0.9983$, $n = 6$), with a detection limit of 1 μM estimated at a signal-to-noise ratio of 3. The sensitivity of the sensor is calculated by the geometric surface area of the electrode, which was 0.14 μA mM^{-1} mm^{-2}. The performance of the sensor was compared with those of the previous report, and the result had shown in Table 1. Notably, the as-prepared sensor exhibited wider linear response range and comparable detection limit towards the glucose oxidation. This might be attributed to the nanostructure of NSNF provided higher surface area and more exposed active sites, which was

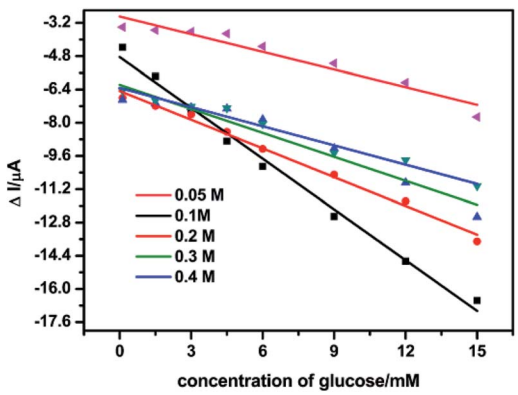

Fig. 4 Linear plots of Δi *vs.* the glucose concentration in the different NaOH solutions with the concentration of 0.05, 0.1, 0.2, 0.3 and 0.4 M on the NSNF/ITO at a scan rate of 50 mV s^{-1}.

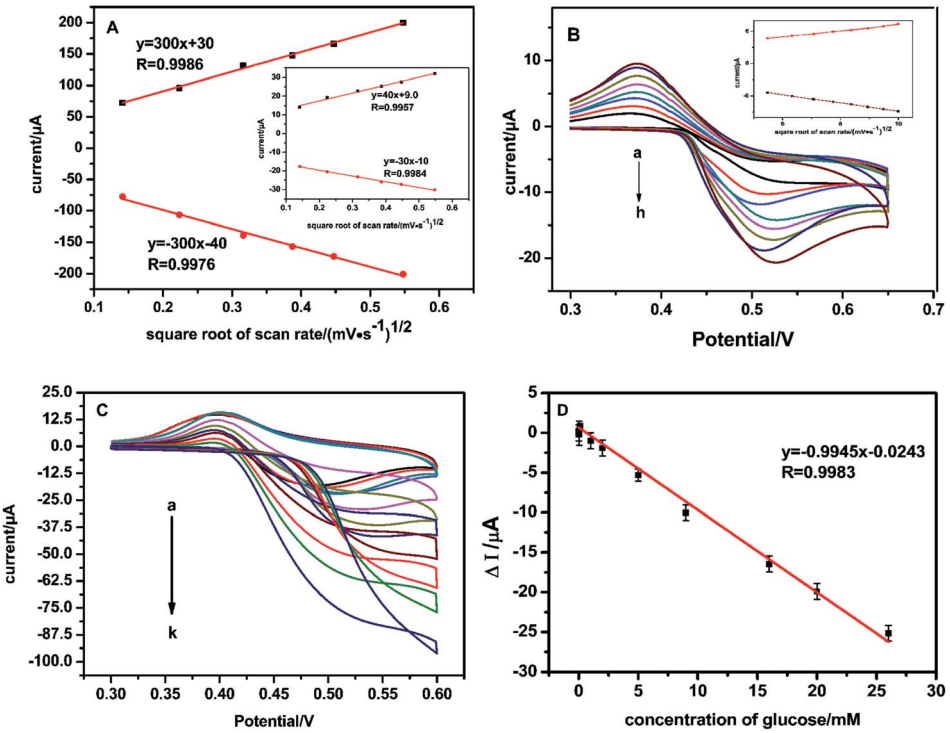

Fig. 5 (A) The linear plots of i_p *vs.* $v^{1/2}$ of NSNF/ITO and blank ITO (the inset). (B) CVs recorded at NSNF/ITO in 0.1 M NaOH containing 1.0 mM glucose, at the scan rate of 30, 40, 50, 60, 70, 80, 90 and 100 mV s^{-1} (from a to h). The inset is the linear plot of i_p *vs.* $v^{1/2}$ induced from the CV curves. (C) CVs recorded the catalysis of NSNF/ITO to different concentrations of glucose (from a to k: 0, 0.01, 0.05, 0.1, 1, 2, 5, 8, 16, 20 and 26 mM) in 0.1 M NaOH at a scan rate of 50 mV s^{-1}. (D) The calibration plot of Δi and the concentrations of glucose ($n = 6$).

Table 1 Comparison of different non-enzymatic electrochemical glucose sensors

Modified electrodes	Linear range/mM	Detection limit/μM	Reference
$Ni(OH)_2$	0.01–0.8	1.2	34
Ni–Co	0.01–2.65	3.79	35
NiO	0.00167–0.42	0.53	36
PPy–NiO	0.01–0.5 and 1.0–20	0.33 5.77	37
rGO/$Ni(OH)_2$	0.015–30	15	38
Ni–rGO	0.001–0.11	—	39
NSNF	0.01–26	1.0	This work

favorable for the diffusion of the electrolyte from solution to all active catalytic sites.[24]

3.6 Selectivity of the glucose sensor

The potentially interfering species such as H_2O_2, AA, CA, UA, maltose, sucrose and fructose usually coexist with glucose in real sample. In order to investigate the selectivity of the glucose sensor, the electrochemical responses of the interfering species were also examined on NSNF/ITO in 0.1 M NaOH solution, as shown in Fig. 6. It was observed that nearly negligible current response was recorded with the addition of 1 mM of each interfering species, only accounting for 0.5–8.0% of the Δi value caused by 1 mM glucose. The result suggested that NSNF/ITO possessed excellent selectivity for the glucose detection.

3.7 Reproducibility and stability of the glucose sensor

The stability and reproducibility of the glucose sensor were also investigated, respectively. It shows good catalytic response reproducibility to the continuous injection of 1 mM glucose for 10 times (RSD = 95%). The long-term stability is also a significant parameter for evaluating a non-enzymatic sensor. The as-prepared glucose sensor was stored in air at room temperature when not in use, and its amperometric response to 1 mM glucose was measured every 5 days within a 30 day period, showing only 4.5% of current loss over this period. Both the evidence above indicated a satisfying stability and good reproducibility of NSNF/ITO for glucose oxidation.

3.8 Analysis of human serum samples

The proposed method was applied to the determination of glucose in human blood serum. The serum samples were obtained from JSCCL. We measured the recovery in healthy human serum samples by adding different concentrations of glucose to 0.1 M NaOH solution containing 10% of human serum. The recovery value of glucose was calculated as 97.6–104.0%, which was presented in Table 2. The relative standard deviations (RSD) are less than 5% for all human blood serum samples, showing a good application prospect.

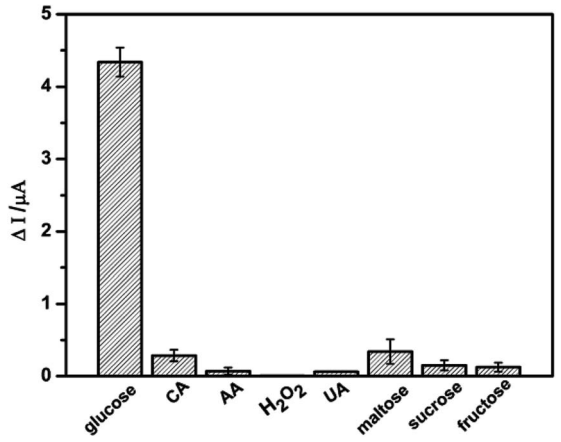

Fig. 6 The Δ*i* responses of NSNF/ITO towards 1.0 mM of glucose, CA, AA, H_2O_2, UA, maltose, sucrose and fructose respectively.

Table 2 The recovery of glucose by standard addition method in real serum samples

Sample	Added concentration/mM	Measured concentration/mM	Recovery/%
1	0.5	0.52	104.0
2	1	0.98	98.0
3	5	4.88	97.6
4	10	10.15	101.5

4. Conclusions

In this paper, we presented a novel enzyme-free electrochemical glucose sensor based on NSNF/ITO, which had a good conductivity, biocompatibility and catalytic activity. In the micro-structure of NSNF, SnO_2 provided the main porous framework components, while NiO showed a good catalytic performance. In addition, the SnO_2 skeleton also improved the monodispersity of NiO nanoparticles and accelerated the electron transfer. The glucose sensor exhibited high sensitivity, low detection limit, long term stability and excellent selectivity in glucose determination. The sensor was further applied to glucose detection in human blood serum samples by standard addition method.

Conflicts of interest

There are no conflicts to declare.

Acknowledgements

This work was financially supported by the National Natural Science Foundation of China (No. 21575064), Natural Science Foundation of Jiangsu Province, China (BK20151535), Jiangsu provincial Key Laboratory of Molecular Biology for Skin Diseases and STIs (2015KF03), and the Six Talent Peaks Project in Jiangsu Province (2016-SWYY-022). This work is also sponsored by Qing Lan Project of Education Department of Jiangsu Province.

Notes and references

1 D. Agustini, M. F. Bergamini and L. H. M. Junior, *Biosens. Bioelectron.*, 2017, **98**, 161–167.
2 C. Nan, Y. Zhang, G. Zhang, C. Dong, S. Shuang and M. M. F. Choi, *Enzyme Microb. Technol.*, 2009, **44**, 249–253.
3 K. Tian, M. Prestgard and A. Tiwari, *Mater. Sci. Eng., C*, 2014, **41**, 100–118.
4 X. Niu, M. Lan, H. Zhao and C. Chen, *Anal. Chem.*, 2013, **85**, 3561–3569.
5 B. Zhan, C. Liu, H. Chen, H. Shi, L. Wang, P. Chen, W. Huang and X. Dong, *Nanoscale*, 2014, **6**, 7424–7429.
6 S. Ci, T. Huang, Z. Wen, S. Cui, S. Mao, D. A. Steeber and J. Chen, *Biosens. Bioelectron.*, 2014, **54**, 251–257.
7 X. Han, Y. Zhu, X. Yang and C. Li, *J. Alloys Compd.*, 2010, **500**, 247–251.
8 J. M. Zen and C. W. Lo, *Anal. Chem.*, 1996, **68**, 2635–2640.
9 L. Q. Chen, X. E. Zhang, W. H. Xie, Y. F. Zhou, Z. P. Zhang and A. E. G. Cass, *Biosens. Bioelectron.*, 2002, **17**, 851–857.
10 R. Wilson and A. P. F. Turner, *Biosens. Bioelectron.*, 1992, **7**, 165–185.
11 X. H. Kang, Z. B. Mai, X. Y. Zou, P. X. Cai and J. Y. Mo, *Anal. Biochem.*, 2007, **363**, 143–150.
12 A. Liu, Q. Ren, T. Xu, M. Yuan and W. Tang, *Sens. Actuators, B*, 2012, **162**, 135–142.
13 Y. Wang, J. Chen, C. Zhou, L. Zhou, Y. Kong, H. Long and S. Zhong, *Electrochim. Acta*, 2014, **115**, 269–276.
14 G. H. Wu, X. H. Song, Y. F. Wu, F. Chen and X. Chen, *Talanta*, 2013, **105**, 379–385.
15 G. Wang, X. He, L. Wang, A. Gu, Y. Huang and B. Fang, *Microchim. Acta*, 2013, **180**, 161–186.
16 P. Si, Y. Huang, T. Wang and J. Ma, *RSC Adv.*, 2013, **3**, 3487–3502.
17 L. Luo, F. Li, L. Zhu, Y. Ding, Z. Zhang, D. Deng and B. Lu, *Colloids Surf., B*, 2013, **102**, 307–311.
18 R. A. Soomro, Z. H. Ibupoto, Sirajuddin, S. T. H. Sherazi, M. I. Abro and M. Willander, *Microsyst. Technol.*, 2016, **22**, 2549–2557.
19 R. A. Soomro, Z. H. Ibupoto, Sirajuddin, M. I. Abro and M. Willander, *Sens. Actuators, B*, 2015, **209**, 966–974.
20 R. Prasad, V. Ganesh and B. R. Bhat, *RSC Adv.*, 2016, **6**, 62491–62500.
21 F. Gentile, E. Battista, A. Accardo, M. Coluccio, M. Asande, G. Perozziello, G. Das, C. Liberale, F. De Angelis, P. Candeloro, P. Decuzzi and E. D. Fabrizio, *Microelectron. Eng.*, 2011, **88**, 2537–2540.
22 Q. Lu, J. Rosen, Y. Zhou, G. S. Hutchings, Y. C. Kimmel, J. G. Chen and F. Jiao, *Nat. Commun.*, 2014, **5**, 32–42.
23 S. R. Wang, J. D. Yang, H. X. Zhang, Y. S. Wang, X. L. Gao, L. W. Wang and Z. Y. Zhu, *Sens. Actuators, B*, 2015, **207**, 83–89.
24 H. Ren, W. Zhao, L. Y. Wang, S. Ok Ryu and C. P. Gu, *J. Alloys Compd.*, 2015, **653**, 611–618.
25 R. Prasad and B. R. Bhat, *Sens. Actuators, B*, 2015, **220**, 81–90.
26 S. K. Meher, P. Justin and G. R. Rao, *ACS Appl. Mater. Interfaces*, 2011, **3**, 2063–2073.

27 Y. B. Mollamahale, Z. Liu, Y. Zhen, Z. Q. Tian, D. Hosseini, L. Chen and P. K. Shen, *Int. J. Hydrogen Energy*, 2017, **42**, 7202–7211.
28 Y. Q. Zhang, Y. Z. Wang, J. B. Jia and J. G. Wang, *Sens. Actuators, B*, 2012, **171–172**, 580–587.
29 L. M. Lu, L. Zhang, F. L. Qu, H. X. Lu, X. B. Zhang, Z. S. Wu, S. Y. Huan, Q. A. Wang, G. L. Shen and R. Q. Yu, *Biosens. Bioelectron.*, 2009, **25**, 218–223.
30 X. M. Chen, Z. J. Lin, D. J. Chen, T. T. Jia, Z. M. Cai and X. T. Wang, *Biosens. Bioelectron.*, 2010, **25**, 1803–1808.
31 M. M. Tunesi, R. A. Soomro and R. Ozturk, *J. Mater. Chem. C*, 2017, **5**, 2708–2716.
32 O. Parlak, P. Seshadri, I. Lundström, A. P. F. Turner and A. Tiwari, *Adv. Mater. Interfaces*, 2014, **1**, 1400136.
33 K. Ngamchuea, S. Eloul, K. Tschulik and R. G. Compton, *J. Solid State Electrochem.*, 2014, **18**, 3251–3257.
34 G. Wang, X. Lu, T. Zhai, Y. Ling, H. Wang, Y. Tong and Y. Li, *Nanoscale*, 2012, **10**, 3123–3127.
35 L. Wang, X. Lu, Y. Ye, L. Sun and Y. Song, *Electrochim. Acta*, 2013, **114**, 484–493.
36 S. Ci, T. Huang, Z. Wen, S. Cui, S. Mao, D. A. Steeber and J. Chen, *Biosens. Bioelectron.*, 2014, **54**, 251–257.
37 M. Tilagam, S. Mohamad and Y. Alias, *Synth. Met.*, 2015, **207**, 35–41.
38 P. Subramanian, J. Niedziolka-Jonsson, A. Lesniewski, Q. Wang, M. Li, R. Boukherroub and S. Szunerits, *J. Mater. Chem. A*, 2014, **15**, 5525–5533.
39 Z. Wang, Y. Hu, W. Yang, M. Zhou and X. Hu, *Sensors*, 2012, **12**, 4860–4869.